1 **Time varying changes and uncertainties in the CMIP6 ocean carbon sink from global to local scale**

2 Parsa Gooya[1], Neil C. Swart[2,1], Roberta C. Hamme[1]

3 [1]School of Earth and Ocean Sciences, University of Victoria, Victoria, BC, V8P 5C2, Canada

4 [2]Canadian Centre for Climate Modelling and Analysis, Environment and Climate Change Canada, Victoria, BC,

5 V8W 2P2, Canada

6 *Correspondence to*: Parsa Gooya (parsa.g76@gmail.com)

7 **Abstract.** As a major sink for anthropogenic carbon, the oceans slow the increase of carbon dioxide in the

8 atmosphere and regulate climate change. Future changes in the ocean carbon sink, and its uncertainty at a global

9 and regional scale, are key to understanding the future evolution of the climate. Here we report on the changes and

10 uncertainties in the historical and future ocean carbon sink using output from the Coupled Model Intercomparison

11 Project Phase 6 (CMIP6) multimodel ensemble and compare to one observation based product. We show that the

12 ocean carbon sink is concentrated in highly active regions - 70 percent of the total sink occurs in less than 40

13 percent of the global ocean. High pattern correlations between the historical and projected future carbon sink

14 indicate that future uptake will largely continue to occur in historically important regions. We conduct a detailed

15 breakdown of the sources of uncertainty in the future carbon sink by region. Consistent with CMIP5 models,

16 scenario uncertainty dominates at the global scale, followed by model uncertainty, and then internal variability. We

17 demonstrate how the importance of internal variability increases moving to smaller spatial scales and go on to show

18 how the breakdown between scenario, model, and internal variability changes between different ocean regions,

19 governed by different processes. Using the CanESM5 large ensemble we show that internal variability changes

20 with time based on the scenario, breaking the widely employed assumption of stationarity. As with the mean sink,

21 we show that uncertainty in the future ocean carbon sink is also concentrated in the known regions of historical

22 uptake. Patterns in the signal-to-noise ratio have implications for observational detectability and time of emergence,

23 which we show to vary both in space and with scenario. We show that the largest variations in emergence time

24 across scenarios occurs in regions where ocean sink is less sensitive to forcing - outside of the highly active regions.

25 In agreement with CMIP5 studies, our results suggest that to detect changes in the ocean carbon sink as early as

26 possible, and to efficiently reduce uncertainty in future carbon uptake, modelling and observational efforts should

27 be focused in the known regions of high historical uptake, including the Northwest Atlantic and the Southern

28 Ocean.

1. Introduction

Recent increases in greenhouse gases have trapped additional heat relative to the pre-industrial era and raised Earth's average temperature. Carbon dioxide (CO_2) is the primary driver of eglobal warming in the industrial period (Masson-Delmotte et al., 2021). The concentration of atmospheric CO_2 has increased from approximately 277 parts per million (ppm) in 1750 (Joos et al., 2008), the beginning of the Industrial Era, to 409 ppm in 2019. However, less than half of the CO_2 emitted by anthropogenic activity has remained in the atmosphere. The remaining CO_2 was taken up by the natural carbon sinks of the ocean and the terrestrial biosphere. Specifically, the global ocean absorbed ~26% of the total CO_2 emissions during 2011-2020 (Friedlingstein et al., 2021).

The ocean's capacity to absorb anthropogenic CO_2 is not uniformly distributed (McKinley et al., 2016, Sarmiento et al., 1998). Despite increasing atmospheric CO_2 concentrations, the air-sea CO_2 flux does not change much in the subtropical gyres. The regions where ocean carbon uptake notably increases are those with strong exchange between the surface and the deep ocean (Ridge and McKinley, 2021; Frölicher et al., 2015; McKinley et al., 2016). This response of the ocean carbon sink to increasing atmospheric CO_2 levels consists of changes in both the anthropogenic and the natural carbon sink (Crisp et al. 2022, McKinley et al. 2020, Hauk et al., 2020, Gruber et al. 2019, Frolicher at al, 2015). Even within regions there are large variations in the dominant mechanisms and the direction of the carbon sink. In the Southern Ocean, for instance, the spatial superposition of natural and anthropogenic CO_2 fluxes leads to a relatively strong uptake band between approximately 55°S and 35°S (Gruber et al., 2019). However, south of the Polar Front (55°S), the different estimates agree less well (Gruber et al., 2019). Supported by measurements based on biogeochemical floats (Bushinsky et al., 2019; Gray et al., 2018; Williams et al., 2018), Gruber et al. (2019) argue that the region was most likely a small source in 2019.

Earth System Models (ESMs) are the primary tool for projecting the future evolution of carbon in the climate system. However, quantitative projections from ESMs are subject to considerable uncertainty, particularly at regional and local scales (Friedrich et al., 2012; Frölicher et al., 2014; Hauck et al., 2015; Roy et al., 2011; Tjiputra et al., 2014; Terhaar et al., 2021) where less averaging is done and different individual mechanisms dominate different regions. Projection uncertainty varies with lead time, spatial averaging scale, and from region to region (Lovenduski et al., 2016; Schlunegger et al., 2020). For example, Lovenduski et al. (2016) showed a spatially heterogeneous pattern of projection uncertainty in CO_2 flux projections over 17 ocean regions for CMIP5 models. Furthermore, by comparing uncertainty at the global scale to the scale of the California Current System, they show that uncertainty is higher at smaller scales. Schlunegger et al. (2020) further shows different partitioning of

60   uncertainty for 10 ocean basins at the year 2050. All said, if ESMs are to be used to quantify future changes in

61   ocean carbon uptake, especially across shorter timescales and at regional spatial scales, and to inform observational

62   campaign planning, their uncertainties must be well known and well understood (Lovenduski et al., 2016).

63

64   A systematic characterization of projection uncertainty has become possible with the advent of the Coupled Model

65   Intercomparison Project (CMIP), as a number of climate models of similar complexity provided simulations over

66   a consistent time period and with the same set of emissions scenarios (Lehner et al., 2020). There are three main

67   types of uncertainty in climate model projections, as described by Hawkins and Sutton (2009) (hereafter HS09):

68

69   **Uncertainty due to internal variability:** Internal variability is the unforced natural climate variability resulting

70   from the internal processes in the climate system. Modes such as the El Niño–Southern Oscillation, North Atlantic

71   Oscillation, Atlantic Multidecadal Oscillation, Pacific Decadal Oscillation, and Southern Annular Mode (SAM)

72   contribute to this internal variability. Internal variability also includes variability that acts on shorter time and

73   spatial scales, such as submesoscale and mesoscale ocean features (Frolicher et al., 2016). The real world follows

74   only one of an infinite possible number of *realizations* of internal variability, and due to its chaotic nature, the

75   future evolution of internal variability is not predictable beyond short timescales (Somerville, 1987; Lorenz, 1969).

76   Climate model simulations do not attempt to reproduce the exact observed evolution of internal variability, but

77   produce their own, unique realizations that aim to capture the correct statistics of this variability. Hence, our

78   analysis must account for internal variability, both when comparing historical model simulations to observations,

79   and when considering uncertainties in the future ocean carbon sink. In HS09, a fourth-order polynomial fit to

80   simulated global and regional temperature timeseries represented the forced response, while the residual from this

81   fit represented the internal variability. There is thus, an assumption of stationarity (constant in time) in their method.

82   Moreover, this approach could possibly conflate internal variability with the forced response in cases where low-

83   frequency (decadal-to-multidecadal) internal variability exists, or when the forced signal is weak, which makes the

84   statistical fit a poor estimate of the forced response (Kumar and Ganguly, 2018). In this study, we instead use a

85   Single-Model Initial-condition Large Ensemble (SMILE) to robustly quantify the internal variability across time

86   and scenarios using ensemble statistics (Lehner et al., 2020). A SMILE is an ensemble of model realizations that

87   each starts from different initial conditions but uses the same model and forcing, and provides representations of

88   the climate system that are equivalent except for internal variability.

89   **Uncertainty due to model structure:** Models differ in their resolution, structure, numerics, and parameterization

90   of processes. These differences cause models to respond differently to the same forcing. For example, the CMIP5

model simulations run under Representative Concentration Pathway 8.5 (RCP8.5) project a wide range of cumulative anthropogenic carbon storage by 2100 (320–635 Pg-C) (Ciais and Sabine, 2013) due to both internal variability and model uncertainty (Lovenduski et al., 2016).

Uncertainty due to emission scenario: The future of the climate system depends on human activity and our emission of climate active gases that change radiative forcing. Future emissions are highly uncertain, given our inability to project the complex changes in society and technology upon which they depend. As a result, future simulations are run with a range of possible "scenarios" for how future emissions (or atmospheric concentrations) will evolve under different socioeconomic storylines. These scenarios are prescribed via the internationally coordinated experiments organized by the Coupled Model Intercomparison Project. Since the future emission trajectory is unknown, these future simulations are referred to as projections, rather than predictions. Projections of future ocean carbon uptake from ESMs are greatly influenced by the choice of emission scenario (Lovenduski et al., 2016). For example, cumulative ocean carbon uptake from 1850 is projected to saturate at approximately 290 $\pm$ 30 GtC under ssp126, and to reach 520 $\pm$ 40 GtC by 2100 under ssp585 for CMIP6 models (Canadell et al., 2021).

Together with the patterns of changes in the sink, the patterns of internal variability allow for an assessment of the required timescales for detection of changes in the ocean carbon sink. Detection means that we can robustly separate the forced signal from internal variability (McKinley et al., 2016). Detectability can be assessed using Time of Emergence (TOE; Hawkins and Sutton, 2012; Lovenduski et al., 2016; McKinley et al., 2016; Rodgers et al., 2015; Schlunegger et al., 2020 & 2019). For example, McKinley et al. (2016) and Schlunegger et al. (2019) showed that the forced signal of increasing ocean carbon uptake is not detectable in the Ekman convergence regions of the subtropical gyres. Schlunegger et al. (2020) builds on that using four large ensembles of CMIP5 ESM simulations with two forcing scenarios to show that air-sea CO_2 flux TOEs show strong agreement between the large-ensembles not just for global and regional scales but also locally and spatially. Their use of only four models and two scenarios however, potentially underestimates the contribution of model and scenario uncertainty.

Here, we build on previous work using CMIP6 models. We make use of an ensemble of 13 models to better capture model uncertainty in the response to different forcing (scenarios) and three scenarios to represent a wider range of future possibilities including a strong mitigation scenario. We start by analysing the regional patterns of historical ocean carbon uptake and how they are projected to change in the future (Sect. 3.1). We estimate internal variability from a comprehensive SMILE, avoiding the stationarity assumption common in previous work, which we show is

violated. Then, we examine the partitioning among different sources of uncertainty (Sect. 3.2) and provide a novel analysis of how the three sources of variability change across the full continuum of scales (Sect. 3.3). Having Shown how the uncertainty and distribution among sources differ based on scale of integration and region of interest, we analyse local patterns of uncertainty by the source (Sect. 3.4). The final section explores the detectability of the model projected signal given the uncertainty imposed by internal variability. We report on the scenario-dependent Time of Emergence, using a scenario specific measure of internal variability in order to make useful suggestions for future observations.

2. Data and Methods

2.1 Model Data Selection

Here we use results from models selected from the 6th Coupled Model Intercomparison Project (CMIP6; Eyring et al., 2016). Models are chosen based on availability, meaning all models that provided at least one realisation for air-sea CO_2 flux (fgco2) for the CO_2 concentration driven experiments of interest. One realization of each model over the historical period and three scenarios that represent the low (ssp126), mid (ssp245), and high (ssp585) ranges of future atmospheric CO_2 concentrations are analysed. A total of 16 models met these criteria, out of which 3 were excluded as outliers (see section S1 in the Supplements). To maintain equal sampling, only one realization of each model was selected, except when specifically using the large ensembles to assess internal variability. Finally, since the ocean component of the models may be on different grids, all model data were remapped to a regular one-by-one-degree grid and a 10 year running mean filter was applied to the time-series. We did not account for potential drift in the models. However, the drift is known to be small in the models compared to the historical trends for CMIP5 models (Hauck et al, 2020). For 11 of our CMIP6 models for which piControl runs are available, on average, the drift is more than one order of magnitude smaller than the change in the model scenario with the smallest trend over the 21st century, on the global scale.

2.2 Sources of uncertainty

Total uncertainty is composed of internal, model, and scenario uncertainty in equation 1, which assumes that each of these sources is independent. Here, each source of uncertainty is considered as a function of time (t) and location (l) (Lovenduski et al., 2016):

$$(1)$$

$$U_T{}^2(t, l) = U_I{}^2(t, l) + U_M{}^2(t, l) + U_s{}^2(t, l)$$

where $U_T(t, l)$ is total uncertainty, $U_I(t, l)$ is internal variability, $U_M(t, l)$ is model uncertainty, and $U_S(t, l)$ is scenario uncertainty. The fractional uncertainties for each source are calculated as $\frac{U_I^2}{U_T^2}$, $\frac{U_M^2}{U_T^2}$, and $\frac{U_S^2}{U_T^2}$ (Lovenduski et al., 2016).

HS09 assume $U_I(t, l)$ to be constant in time (stationary) and use a 4th degree polynomial fit to measure internal variability as the spread over time and scenario of the residuals for each model's signal relative to the fitted signal. We show in the Supplements (see section S2) that internal variability depends on time and scenario, violating the commonly used assumption of stationarity. Using a SMILE allows us to account for these variations without having to make any assumptions about distribution or stationarity of variability (Frolicher et al., 2015; Schlunegger et al., 2020). Here we estimate internal variability as two times the standard deviation of the annual carbon sink across 50 realizations from a Single Model Initial Condition Large-ensemble based on CanESM5 (Eq. 2):

$$U_I(t, l) = 2\sqrt{\frac{1}{Ns}\sum_{s=1}^{N_s} \text{Var (CanESM5 Large Ensemble)}} \qquad (2)$$

where s indicates each scenario (Ns is the number of scenarios) and Var indicates the variance over the large ensemble of CanESM5. In the CanESM5 SMILE, each realization starts from different initial conditions which are drawn from points separated by 50 years in the piControl simulation. Thus, the spread across the realizations gives a robust estimate of the internal variability, including sampling over longer term ocean variability.

Previous studies have also used SMILEs to estimate variability (Frolicher et al., 2015; Schlunegger et al., 2020), although they used either a limited ensemble size or single scenario. We show in the Supplements (Fig. S2), that a sufficiently large ensemble size is needed to capture internal variability, and that internal variability depends on the scenario. In the ideal case, if every CMIP model provided sufficiently large SMILEs for each scenario, an ensemble mean estimate of the variability could be obtained and would represent a best estimate (but still possibly biased compared to the real world). However, only a handful of CMIP6 models produced multiple ensemble members.

179 We selected the CanESM5 SMILE as it is the only model that has a large enough ensemble over the entire timeline
180 and set of experiments to make estimate internal variability robustly and across scenarios.

181

182 The use of a single model to estimate the scale of internal variability leads to some uncertainty in our estimates, as
183 models do not agree perfectly with each other on the variability. Nonetheless, over the historical period, variability
184 between large ensembles from three models that have enough ensemble members is within 10%, on the global scale
185 (Fig S3). Differences will be larger at smaller scales; however, the general patterns of the magnitude of internal
186 variability (see Fig. S4) are in good agreement across models and are consistent with known regions of high
187 variability in the observed ocean, validating our use of the CanESM5 SMILE

188

189 Model uncertainty is calculated by taking the variance across the forced signal of all available models for each
190 scenario, averaging over the three scenarios, and then reporting twice the square root of the result (Eq. 3).

$$191 \quad U_M(t, l) = 2 \sqrt{\frac{1}{Ns} \sum_{s=1}^{N_s} \text{Var}_m \big(F(m, s, t, l) \big)} \qquad (3)$$

192 where Var_m means the variance taken across different models for individual times and scenarios, m indicates each
193 model, and t stands for time. $F(m, s, t, l)$ is the forced signal and can be related to each realization as follows:

194

$$195 \quad T(m, s, t, l) = F(m, s, t, l) + R(m, s, t, l) \qquad (4)$$

196

197 Where, $T(m, s, t, l)$ represents the reported output, i.e. each realization, but must be corrected for internal
198 variability. $R(m, s, t, l)$ is the residual from the forced signal caused by internal variability. Here, the variance in
199 the forced signal across all models is calculated by correcting the total variance across all models' one realization
200 for the variance caused by internal variability. The corrections are done by subtracting the variance across the same
201 number of CanESM5 ensemble members as the multi-model ensemble (13 members) from the variance across the
202 one realization of all of the 13 models. For this correction only, the sample sizes (13) are kept the same so that the
203 internal variability removed from the variance across the models' first realizations is not overestimated by a well
204 sampled 50-member ensemble (see section S3 in the Supplements).

205

206 U_s (t, l) is the scenario uncertainty. Scenario uncertainty is measured as twice the standard deviation (square root
207 of variance) across scenarios of the multi-model mean signal (Eq. 5).

208

$$U_S(t,l) = 2\sqrt{\mathrm{Var}_m\left(\frac{1}{N_m}\sum_{m=1}^{N_m} T(m,s,t,l)\right)} \qquad (5)$$

where N_m is the number of models. The multi-model mean across the first realizations of the 13 models gives the multi-model forced response and does not require correction for internal variability as done for model uncertainty before.

We conduct analysis on three different scales: single grid point (one-degree resolution), regional, and global. When regional and global analysis is done, the dependence on location is taken away by averaging over that region or the whole global ocean.

2.3 Time of Emergence (TOE)

In order to know when the forced response is distinguishable from internal variability, TOE is calculated following the approach of McKinley et al. (2016). The time of emergence is the first year when the multi-model mean anomaly is larger than internal variability – approximated by two times the standard deviation across the 50 member CanESM5 ensemble - for five consecutive years (the first year of this five-year period is reported as the time of emergence). The result is reported at each grid point for the 10-year running mean smoothed anomaly relative to the 1995-2015 mean (detection of a change relative to the current state of the ocean).

2.4 Scale Dependence

Finally, the scale dependence of the sources of uncertainty is measured at year 2050 using ssp245 for internal variability and model uncertainty, and using all scenarios for scenario uncertainty. The analysis is done by moving a sliding sample window of a given area across the earth, and then repeating with a larger and larger window until all scales from <100 km^2 to the whole Earth are considered. For each source of uncertainty and averaging scale, the average for all rectangles across the globe is reported, where each rectangle contains the same ocean area.

3. Results and Discussion

3.1 Global Analysis

The pattern of the carbon sink in the CMIP6 multi-model ensemble mean from the historical experiment over 1995-2015 matches that of the Landschützer (2016) Self Organizing Map - Feed Forward Neural Network (SOM-FFN) observation-based data product estimate (correlation coefficient of 0.84, compare Figs. 1a and 1b). We use the multi-model mean response to external forcing as a more robust estimate of the forced climate signal than the response of any single model (Tebaldi & Knutti, 2007). Unlike in ESMs, the observation-based product only represents the one realization of the real world, which includes internal variation, and is therefore not directly equivalent to the forced signal. However, the comparison to the 20 year mean multi-model mean still informs us about the degree of agreement between the two products. When compared to the observation-based data product, the CMIP6 multi-model mean shows a larger sink (positive flux) in the North Atlantic and North and North-West Pacific but a smaller sink in the Southern Ocean (Fig 1a, b). Additionally, the observation-based data product shows a larger source in the Equatorial Pacific and Indian Ocean than the CMIP6 multi-model ensemble.

While most of the global ocean shows a net sink relative to the pre-industrial era, the largest change takes place in some highly active regions such as the subpolar North Atlantic, Southern Ocean, Eastern Equatorial Pacific, and western boundary currents of the mid-latitude gyre systems in the Pacific and Atlantic Oceans (Fig. 1c). These regions of largest change in the carbon sink (anthropogenic plus changes in the natural carbon sink) are the regions where there is a surface-depth connectivity as the air–sea flux of anthropogenic carbon is fundamentally limited by the rate of surface-to-depth transport (Graven et al., 2012; Ridge and McKinley 2021). These results for CMIP6 models are consistent with those for CMIP5 models shown by McKinley et al. (2016) and earlier studies such as Sarmiento et al. (1998). Here, we provide a new metric for quantifying these highly active regions. We find that for all three scenarios and both mid-21st century (2040-2060 mean) and late- 21st century (2080-2100 mean) time periods (with the exception of ssp126 late-century where strong mitigation of anthropogenic CO_2 emissions results in broad patterns of negative anomalies), approximately 70% of the changes in the sink relative to the preindustrial area takes place in less than 40% of the global ocean (see Supplement Fig. S7 and section S5).

The regions of largest future carbon uptake, relative to the 1995-2015 mean, are within the same highly active regions responsible for most of the uptake over the historical period. The correlation coefficients at the top of each panel in Fig. 1 (except 1b) represent the pattern correlation between future absolute anomalies, relative to 1995-2015, and anomalies in 1995-2015, relative to the pre-industrial era. The high correlations indicate that regions that

have been most active in carbon sequestration since the pre-industrial era are the same regions that will continue to change most into the future, particularly with larger increases in atmospheric CO_2 (ssp585). Our results support the findings of Wang et al. (2016) who showed that projected future air-sea CO_2 fluxes are strongly associated with simulated historical air-sea CO_2 fluxes. This confirms that the historical state is a good predictor for the future state (Wang et al., 2016) not only in terms of magnitudes of the sink, but also in the spatial pattern.
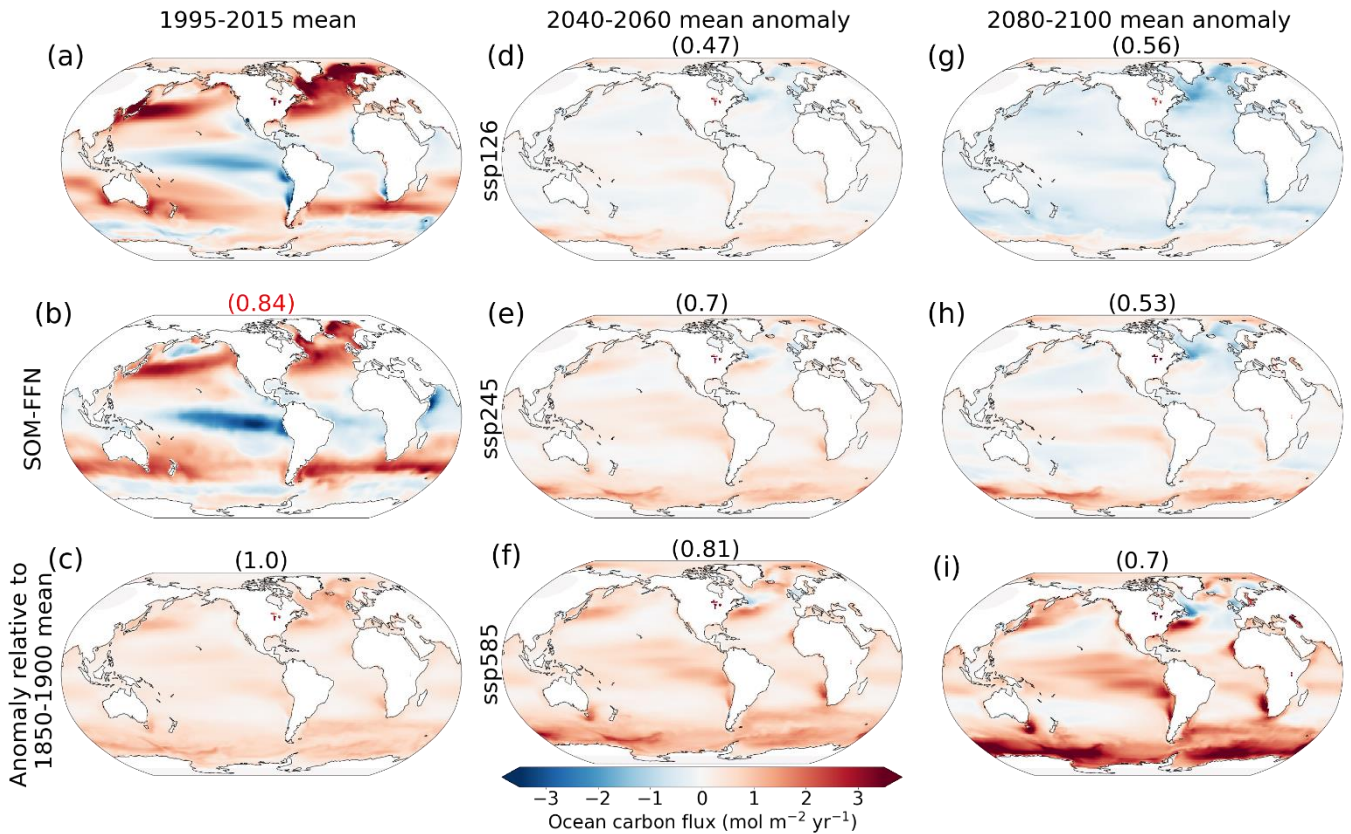
Figure 1- CMIP6 multi-model mean maps of carbon sink and sink anomalies using one realization of each model. Columns represent different time periods, being the recent time (1995-2015 mean), mid-century (2040-2060 mean), and late-century (2080-2100 mean). Note: the sink is positive into the ocean. The first column shows (a) the CMIP6 ensemble mean air-sea CO_2 flux over 1995-2015, (b) Landschützer et al. (2016) SOM- FFN product, and (c) the CMIP6 ensemble mean flux anomaly relative to the 1850-1900 mean. Other panels are anomalies relative to the 1995-2015 multi-model mean (panel a). Panels d through i show different scenarios. Numbers above each map are correlation coefficients between the absolute value

of the change relative to 1995-2015 with the 1995-2015 anomaly map relative to the pre-industrial era in panel c, except the red number at the top of panel b that is the correlation coefficient with this panel and panel a.

The multi-model mean sink anomalies for two future periods, 2040-2060 and 2080-2100, show how the sink is projected to evolve, relative to 1995-2015, according to time and choice of emission scenario (Fig. 1d-i). The regional patterns show mostly positive anomalies at mid-century with largest changes in the higher emission scenarios (ssp585). Towards the end of the century, however, broader patterns of negative anomalies are expected in ssp126, as emissions turn negative in the late-century in this scenario. The largest absolute values of anomalies are still within the same highly active regions discussed before with surface-depth connectivity regardless of it being positive or negative. The late-century anomalies are predominantly positive in ssp585 which corresponds to the highest emission scenario (continuing to grow larger compared to the mid-century), while ssp245 is somewhere in between, with regions of positive and negative anomalies. Under ssp245, as CO_2 emissions decrease and atmospheric CO_2 start to level off, the intensity of uptake decreases in the midlatitude western boundary currents and subpolar North Atlantic in the late-century, and anomalies in the Eastern Equatorial Pacific also decrease, compared to the mid-century. The globally integrated ocean carbon uptake rates are summarized in Table 1.
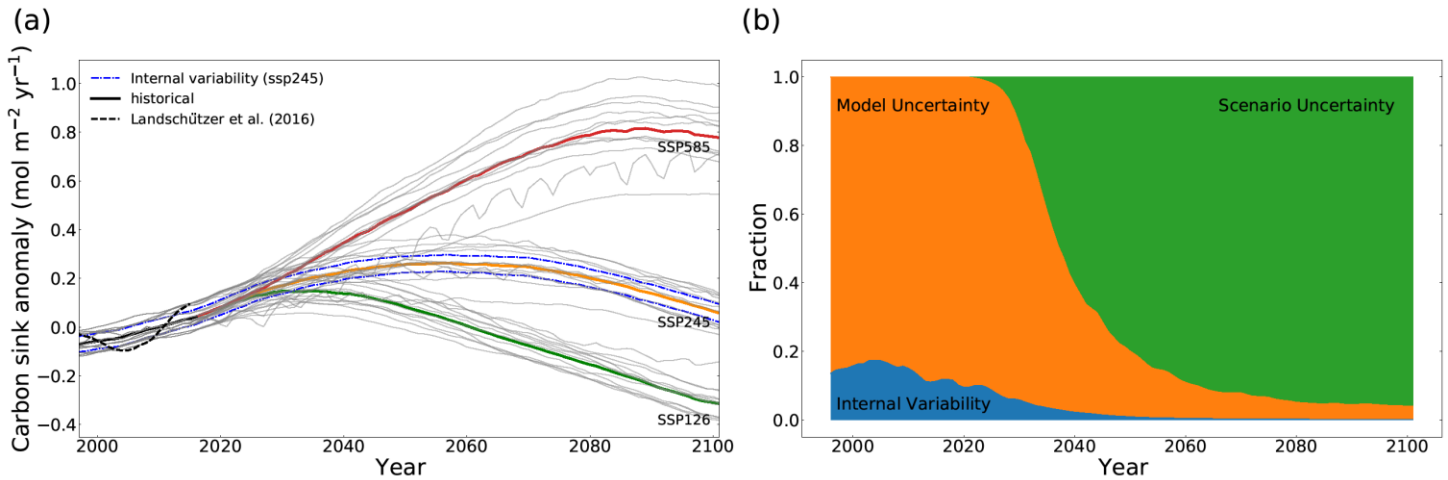
Figure 2- (a) Thick lines are multi-model means of the global mean ocean carbon sink anomaly timeseries relative to 1995-2015. Individual models are plotted as thin grey lines in the background. The black dashed line shows the Landschützer et al. (2016) SOM-FFN product. Both models and SOM-FFN timeseries are smoothed with a 10-year running mean. The blue dashed lines show internal variability for ssp245. (b) Timeseries showing the breakdown of uncertainty to different sources with time for the global ocean carbon sink anomaly. The internal and model uncertainty are averaged for different scenarios.

	Scenario	1995-2020	2020-2040	2040-2060	2060-2080	2080-2100
Anomaly (range)	**ssp126**		0.13 (0.05 – 0.21)	0.07 (-0.02 – 0.16)	-0.08 (-0.14 - -0.01)	-0.24 (-0.3 - -0.12)
	ssp245	0.00 (-0.06 – 0.06)	0.17 (0.08 – 0.24)	0.25 (0.11 – 0.36)	0.23 (0.09 – 0.33)	0.13 (0.02 – 0.21)
	ssp585		0.22 (0.11 - 0.30)	0.49 (0.29 – 0.62)	0.71 (0.45 – 0.90)	0.80 (0.54 – 1.00)
Internal (model) Uncertainty	**ssp126**		0.033 (0.11)	0.034 (0.11)	0.035 (0.10)	0.036 (0.11)
	ssp245	0.032 (0.08)	0.032 (0.11)	0.034 (0.14)	0.037 (0.14)	0.036 (0.12)
	ssp585		0.033 (0.13)	0.037 (0.2)	0.045 (0.26)	0.043 (0.27)
	Average	0.032 (0.08)	0.033 (0.12)	0.035 (0.16)	0.039 (0.18)	0.038 (0.18)

Table 1- CMIP6 multi-model mean globally averaged carbon sink anomalies (with ranges within the 20-yr period in parentheses) relative to the 1995-2015 mean (in mol-C m^{-2} yr^{-1}) and internal variability from CanESM5 (with model uncertainty in parentheses) for the globally averaged ocean carbon sink anomalies for the three scenarios and the average values across scenarios.

The trends in the global mean ocean carbon sink anomalies over 1995-2015 are statistically consistent between the CMIP6 multi-model ensemble mean and the Landschützer et al. (2016) observation-based data product (Fig. 2-a), based on the test from Santer et al. (2008; see Supplements section S5). However, the SOM-FFN based time-series shows a larger multi-decadal variability (variations in the 10-year running mean timeseries on top of the trend) than seen in individual model realizations, and is larger than the range of internal variability estimated from the CanESM5 SMILE. The difference could be due to either overestimation of internal variability by the SOM-FFN method, or underestimation of the internal variability from the ESMs. Given that on regional scales the SOM-FFN data is within the range of internal variability projected by the CMIP6 large-ensemble of CanESM5 (see Sect. 3.3), and that there are significant gaps in the spatial and temporal sampling that underlies the Landschützer et al. (2016) estimate, it seems plausible that the discrepancy is largely due to overestimation of internal variability on the global scale by the SOM-FFN technique. This is consistent with the findings of Gloege et al. (2021), which showed that, globally, the magnitude of decadal variability is overestimated by 21% by the SOM-FFN technique, attributed to the amount of data filling.

On the global scale, model uncertainty is the dominant source of uncertainty in the historical period, but scenario uncertainty comes to dominate later (Fig. 2b). Over the 1995-2020 period, model uncertainty explains around 85% of the total uncertainty. Scenario uncertainty becomes the dominant source after 2040, explaining almost 40% of the total uncertainty at that time and more than 90% by the end of the century. Internal variability explains 15% at the start of the century but only around 1% by the end. It is worth mentioning that the decreased share of uncertainty associated with model and internal variability do not mean that model or internal variability decrease in an absolute sense; rather, their importance relative to scenario uncertainty declines. These results regarding the importance of model and scenario uncertainties for multidecadal projections, and dominance of scenario uncertainty with time agree with previous studies using CMIP5 models (Lovenduski et al., 2016; Schlunegger et al., 2020).

Absolute internal and model uncertainty of the global carbon sink change with time, based on the scenario (Table 2, Fig. S3). High emission scenarios such as ssp585 show a larger change for both internal and model uncertainty where the forcing is stronger (Fig. S3). When averaged for the three scenarios, a constant increase in the magnitudes of both model and internal variability is seen through the century until 2080-2100 when the values either do not change or decrease slightly (Table 1). Model uncertainty more than doubles towards the end of the century compared to 1995-2015 on average for different scenarios. This is consistent with Lovenduski et al. (2016) who argues that the increase is due to difference in climate sensitivities between models that manifest more strongly with time (and hence cumulative emissions). Additionally, the dependence of internal variability on the scenario is

349   an interesting result. Future SMILEs from multiple models will allow evaluation of the degree of dependence and

350   the driving mechanisms of such changes with time based on the forcing (scenario). Our result of internal variability

351   dependence on scenario implies that the time of emergence of a signal out of internal variability will be affected

352   by changes in the internal variability under different future forcing scenarios – which we return to in Section 3.4.

353

354   3.2 Dependence of the sources of uncertainty on spatial scale

355   It is generally accepted that uncertainty and, most importantly, internal variability grow larger as the averaging

356   (integration) scale gets finer, because on larger scales the variability is averaged out. Here, we provide a novel and

357   continuous view of change in variability across scales from the global to grid scale, by measuring how variability

358   changes relative to scale on average (Fig. 3). At the global scale, the dominant source of uncertainty is scenario

359   uncertainty, followed by model and internal variability respectively, consistent with Fig. 2b. However, as the

360   averaging (integration) scale gets finer, model and internal variability grow rapidly, while scenario uncertainty only

361   grows slightly on average (over all regions of this size). At an averaging (integration) scale with an area finer than

362   75 million km^2 (on average around the globe), model uncertainty becomes the dominant source of uncertainty, and

363   at a scale finer than 3 million km^2, internal variability becomes larger than scenario uncertainty. The idea of scale

364   dependence of these uncertainties was tested in Lovenduski et al. (2016) by comparing an area covering the

365   California Current System with the global ocean. Here, we provide a novel analysis on a continuum of scales

366   covering global to regional to local scales. While the results here hold true on average over the globe, scale

367   dependence is partially controlled by the particular region being sampled. Finally, while our estimates of the

368   magnitudes of sources of uncertainty and the cross over points at which the dominance of internal variability over

369   model uncertainty and model uncertainty over scenario uncertainty takes place, depend on the choice of ESMs and

370   the method for calculation of internal variability, the general patterns are unlikely to be model dependent.

371

372
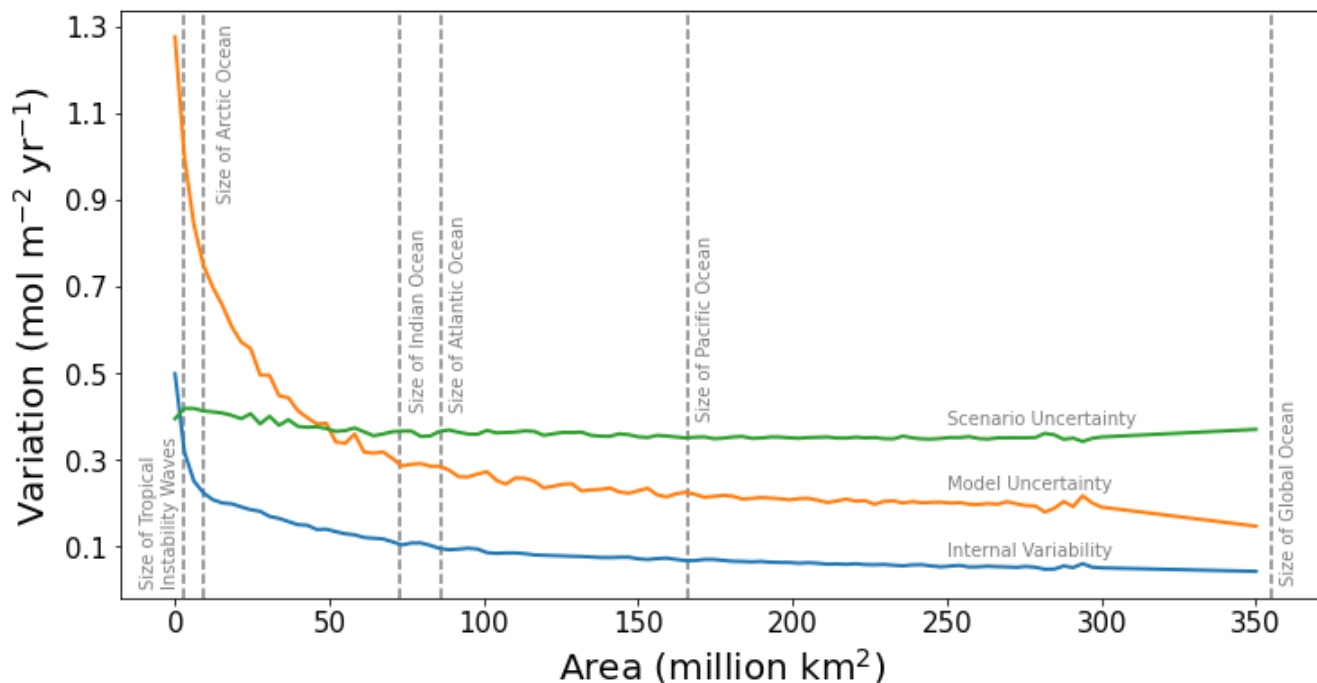
Figure 3- Sources of uncertainty versus area of averaging. Internal variability is based on ssp245 year 2050 of all CanESM5 members. Scenario uncertainty is based on all scenarios of the 13 models at year 2050 and model uncertainty is the corrected standard deviation of our 13 models at year 2050 of ssp245. The values of uncertainties are averaged over all different rectangular areas of each size that can scan the globe. Dashed lines indicate the size of the averaging window and not a specific location.

3.3 Regional Analysis

We further expand on the findings of our analysis of the scale dependence of uncertainty averaged over the globe by repeating the uncertainty breakdown for two specific regions: one between 40°- 60° N in the Northeast Pacific (NE Pacific) between 130°- 160° W and one in the Northwest Atlantic (NW Atlantic) between 40°- 70° W at the same latitude. We chose these regions, first, to be of the similar size, and second to represent very different carbon dynamics. The NW Atlantic region represents a highly active region while the NE Pacific region is more typical of quiescent ocean regions, where the flux anomalies are relatively small.

The variation across scenarios is at all times smaller than internal variability in the NE Pacific (Fig. 4a). This suggests both that it will be difficult to robustly detect any human induced changes in observations of the NEP carbon sink, and that potential future differences relating to choice of mitigation scenarios will not be readily

apparent in the NE Pacific carbon flux. This is true even for the high emission scenarios, because the anomalies are small regardless of scenario (Table 2). We speculate that in the absence of mechanisms providing a pathway to the depth where significant CO_2 accumulation occurs, the surface pCO_2 trend will follow that of the atmosphere closely, causing ΔpCO_2 and therefore air-sea carbon flux to remain fairly constant for all scenarios. In the NW Atlantic however, the deviation across scenarios becomes larger than the internal variability in the early 2060s (Fig. 4c). The response of the region to climate change is dependent on the scenario (Table 2), or, in other words, the amount of carbon dioxide in the atmosphere. This is because the NW Atlantic is a highly active region where the air-sea flux actively responds to the atmospheric CO_2 concentration. The connection to depth allows for surface water to be replaced with water masses whose pCO_2 trend lags behind that of atmosphere. The trend of the CMIP6 multi-model time-series over the historical period is statistically consistent (See Supplements section S5) with that of the observation-based SOM-FFN product, and the multi-decadal variability is within the range of internal variability measured by the CanESM5 large-ensemble in both regions. We note that both of these regions are relatively well sampled, which may lead to more robust estimates of multi-decadal variability in the Landschützer et al. (2016) dataset, and better agreement with the models than seen at the global scale.

Fractional estimates of each source of uncertainty vary with time and have different patterns for these two regions. Internal variability and model uncertainty in the NE Pacific and NW Atlantic are larger by an order of magnitude than at the global scale (Table 2). A lesser importance for scenario uncertainty and greater importance for internal and model uncertainty is apparent in both regions compared to the global scale, in agreement with Schlunegger et al. (2020). Over the period 1995-2020, model uncertainty is the dominant source of uncertainty in both the NE Pacific and NW Atlantic (80-90%), while the remainder is internal variability (Fig. 4bd). Internal variability explains around 25-30% of the total uncertainty in the NE Pacific throughout the century. In the NW Atlantic however, its share drops to 15% by the end of the century. The share attributable to internal variability is much larger during the 21st century in both regions compared to the global scale. Internal variability is larger in the NW Atlantic in an absolute sense (Table 2), but its share of the total uncertainty is larger in NE Pacific (Fig. 4b). The large share of internal variability in NW Pacific indicates the need for sustained observations in the region. Overall, internal variability averaged over the scenarios shows a small increase, but no clear trend in time in both regions until the 2080-2100 period where it decreases, consistent with the global estimates (Table 2). We showed earlier that in the NE Pacific scenarios do not differ because the region is a highly active region (Fig. S7) - scenario uncertainty explains less than 20% of the total uncertainty at the end of the century in the NE Pacific. In the NW Atlantic, scenario uncertainty grows larger with time, becoming 45-50% of total uncertainty by the end of the century. In both regions, model uncertainty is the dominant source of uncertainty in all years.

424

Our regional analysis confirms that while uncertainty and its distribution among sources depends on the spatial scale of integration, the specific location also matters (Lovenduski et al, 2016; Schlunegger et al., 2020). Schlunegger et al., (2020) tested this idea for 10 ocean basins but with different sizes (see their Figure 9). We focused on keeping the sizes similar and analyse a highly active region versus a more quiescent ocean region. The key message here that there is an association with the importance as well as the magnitude of sources of uncertainty with how active the region is in regards to the carbon sink is not sensitive to the use of CanESM5 for estimation of internal variability. Local patterns of uncertainty broken down by source are thus needed to clarify changes based on location.

433

434

435

436

437

438

439

440

441

442

443

444
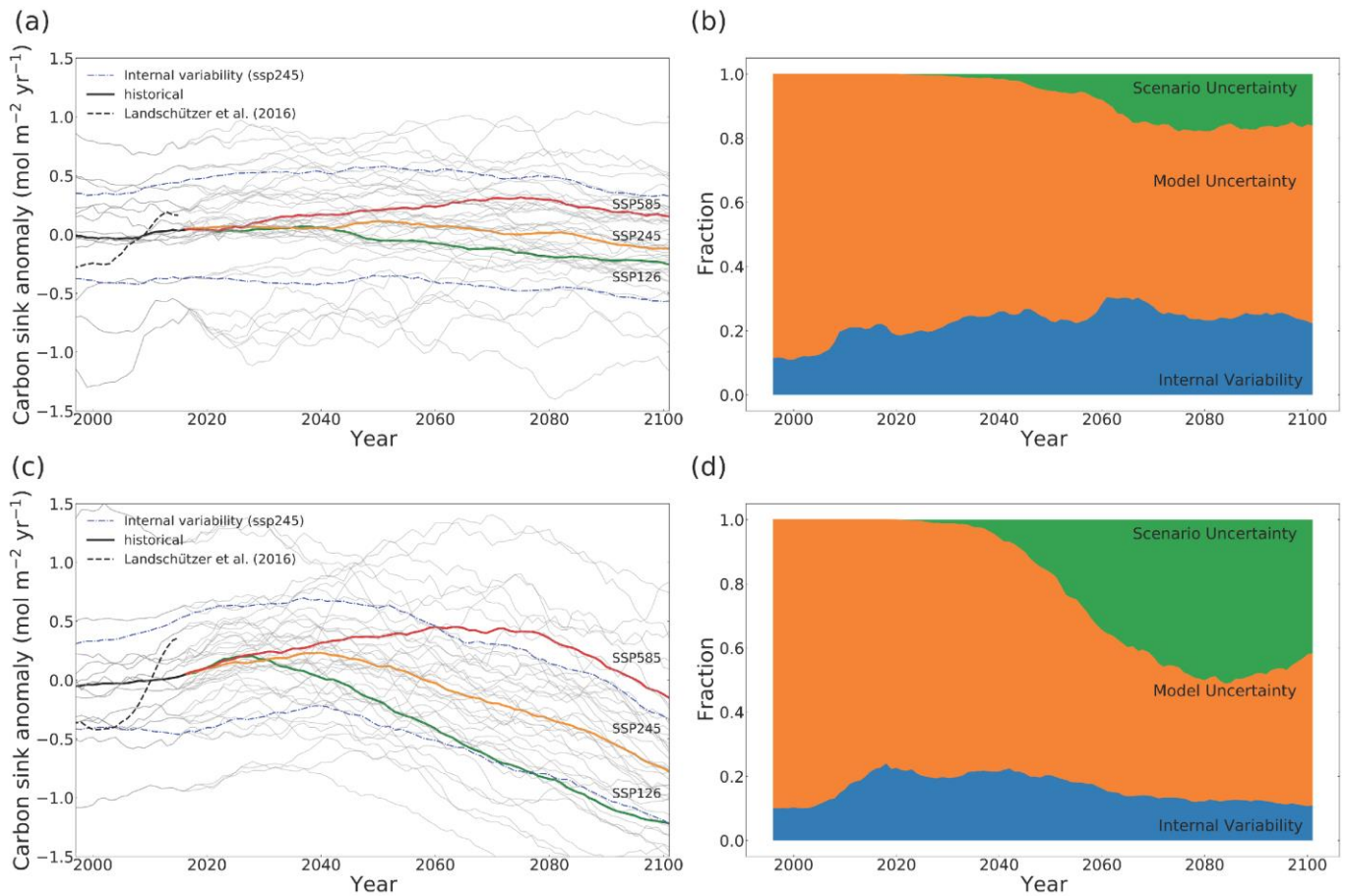
445
446 **Figure 4**- (a), (c) Thick lines are multi-model mean timeseries of anomalies relative to the 1995-2015 mean. All model time-
447 series averaged for the means are plotted in grey lines in the background. The black dashed line shows the Landschützer et
448 al. (2016) SOM-FFN product. The blue dashed line shows the internal variability measured as two times the standard
449 deviation across all 50 members of CanESM5 only for ssp245 here. (b), (d) time-series showing the breakdown of
450 uncertainty to different sources with time. The internal and model uncertainty are averaged for different scenarios. (a), (b)
451 NE Pacific (40-60 °N, 130 -160 °W). (c), (d) NW Atlantic (40 - 60 °N, 40 -70 °W)

452
453
454
455
456
457
458

		Scenario	1995-2020	2020-2040	2040-2060	2060-2080	2080-2100
NE Pacific	**Anomaly (range)**	**ssp126**		0.05 (-0.91 – 0.86)	0.03 (-0.86 – 0.62)	-0.13 (-1.1 – 0.58)	-0.21 (-1.18 - 0.60)
		ssp245	0.00 (-0.98 – 0.76)	0.06 (-0.86 – 0.83)	0.09 (-0.74 – 0.81)	0.03 (-0.65 – 0.60)	0.06 (-0.70 – 0.53)
		ssp585		0.11 (-0.73 - 0.79)	0.21 (-0.61 – 0.86)	0.29 (0.22 – 0.94)	0.2 (-0.25 – 0.98)
	Internal (model) Uncertainty	**ssp126**		0.47 (0.87)	0.43 (0.74)	0.40 (0.81)	0.39 (0.83)
		ssp245	0.39 (0.90)	0.46 (0.87)	0.47 (0.81)	0.48 (0.64)	0.45 (0.53)
		ssp585		0.45 (0.81)	0.47 (0.745)	0.58 (0.55)	0.44 (0.57)
		Average	0.39 (0.90)	0.46 (0.86)	0.46 (0.77)	0.47 (0.70)	0.43(0.67)
NW Atlantic	**Anomaly (range)**	**ssp126**		0.13 (-0.77 – 1.21)	-0.20 (-1.03 – 0.56)	-0.66 (-1.45 – -0.11)	-1.00 (-1.80 - -0.56)
		ssp245	0.00 (-0.97 – 1.31)	0.18 (-0.78 – 1.23)	0.10 (-0.68 – 0.80)	-0.20 (-0.97 – 0.50)	-0.54 (-1.22 – 0.07)
		ssp585		0.23 (-0.70 – 1.20)	0.38 (-0.41 – 1.12)	0.41 (-0.27 – 1.29)	0.10 (-0.70 – 0.96)
	Internal (model) Uncertainty	**ssp126**		0.47 (0.91)	0.47 (0.79)	0.46 (0.78)	0.42 (0.80)
		ssp245	0.43 (1.02)	0.47 (0.96)	0.49 (0.82)	0.49 (0.80)	0.47 (0.79)
		ssp585		0.50 (0.90)	0.51 (0.94)	0.52 (1.00)	0.53 (1.00)
		Average	0.43 (1.02)	0.48 (0.93)	0.49 (0.87)	0.49 (0.88)	0.48 (0.88)

459

Table 2- CMIP6 multi-model mean sink anomalies (with ranges in parentheses) relative to 1995-2015 mean (in mol-C m^{-2} yr^{-1}) and internal variability (with model uncertainty in parentheses) for the three scenarios and their average values in NE Pacific and NW Atlantic.

Consistent with the sink anomaly maps (Fig. 1), the regions that show highest uncertainty for any of the sources in the future, are the same regions that show the largest uncertainties in the historical period (Fig. 5). More importantly, the regions of largest future uptake uncertainty are highly correlated with the historical regions of largest uptake, as shown by the pattern correlation coefficients above each panel. This is a highly significant finding, because it suggests that knowledge of the regions of modern day surface carbon flux anomaly provides us with information about regions of future uptake uncertainty.

Internal variability from CanESM5 is most dominant in mid-latitude eastern boundary upwelling regions and their extensions, in the North Atlantic, in the western boundary currents of the Gulf Stream and Kuroshio and their extensions, and in the Southern Ocean (Fig. 5). There is wide agreement between different models and estimation methods in regions of largest internal variability (Fig. S4). The regions of large internal variability are correlated with the same highly active regions for the sink anomalies discussed earlier (Fig 1c). However, correlation coefficients between internal variability and historical uptake are lower than those seen for scenario and model uncertainty. An increase in internal variability with time is seen mostly in the Southern Ocean, the Arctic Ocean, and boundaries of the gyre systems, while the rest of the ocean does not show a clear change. The maps in Figure 5 are averaged over the three scenarios, which masks the changes to some extent. However, we show in the Supplements (see section S2) that changes in the globally averaged internal variability with time are different for different scenarios.

Model uncertainty is consistently highest in the highly active regions (Figure S7), leading to strong correlation with the anomaly maps of Fig. 1c. In these regions, ocean circulation impacts surface pCO_2 through advection and water mass transformation regionally (Bopp et al., 2015; Toyama et al., 2017) and models have substantial differences in ocean circulation. Ridge and McKinley (2021) suggest that while global surface carbon fluxes and carbon storage are largely similar across ESMs over the historical period, consistent with the external forcing from atmospheric pCO_2 growth being the main driver of the historical sink (McKinley et al., 2020), uncertainties in ocean circulation may become important in the future under a changing trajectory of atmospheric boundary conditions. The model uncertainty is largest in the Southern Ocean consistent with CMIP5 models (Frölicher et al., 2015). Here, mode and intermediate waters are formed, and the complex nature of the sink varies on all time scales (Gruber et al. 2019). Frölicher et al. (2015) note the largest disagreement in ocean carbon uptake between

491   models is in the Southern Ocean because the exact processes governing heat and carbon uptake remain poorly

492   understood. The importance of model uncertainty in the Southern Ocean provides a clear focal point for

493   modelling centers to concentrate their efforts in reducing projection uncertainty.

494   Scenario uncertainty exhibits the largest change with time. This is by construction as the scenarios deviate from

495   each other with time to represent a range of pathways for future socio-economic possibilities in order to assess

496   the long-term impacts of short-term decisions (Riahi et al., 2017). Importantly, the correlation coefficients are

497   highest between scenario uncertainty and the current sink regions, indicating that the same highly active regions

498   are the regions that show the largest divergence among scenarios, and that the sink in most other regions does not

499   respond as strongly to scenario differences. We showed an example of this earlier, where the timeseries of the

500   multi-model signals for the three scenarios did not emerge out of internal variability in the NE Pacific by 2100,

501   whereas they did for the highly actrive region of the NW Atlantic. This shows that with pCO_2 differences across

502   the air-sea interface being the main driver of the sink (Fay & McKinley, 2013; Landschützer et al., 2015;

503   Lovenduski et al., 2007; Mckinley et al, 2020; McKinley et al., 2017), the sink in these active regions evolves as

504   the atmospheric CO_2 concentration changes because ocean processes associated with surface-depth connectivity

505   constantly keep the surface ocean pCO_2 out of equilibrium with the atmosphere. In other words, the surface water

506   in these regions are constantly renewed, mostly through advection and water mass formation, with water masses

507   whose pCO_2 has not increased at the same rate as the atmosphere. Elsewhere, these conditions do not hold true

508   and water at the surface equilibrates with the atmosphere on shorter time scales, decreasing the sensitivity to the

509   projection scenario. These uncertainties are central to the ability to detect human induced trends in observations

510   of the surface ocean carbon flux as well as to assess mitigations or make societal decisions, to which we now

511   turn.

512

513
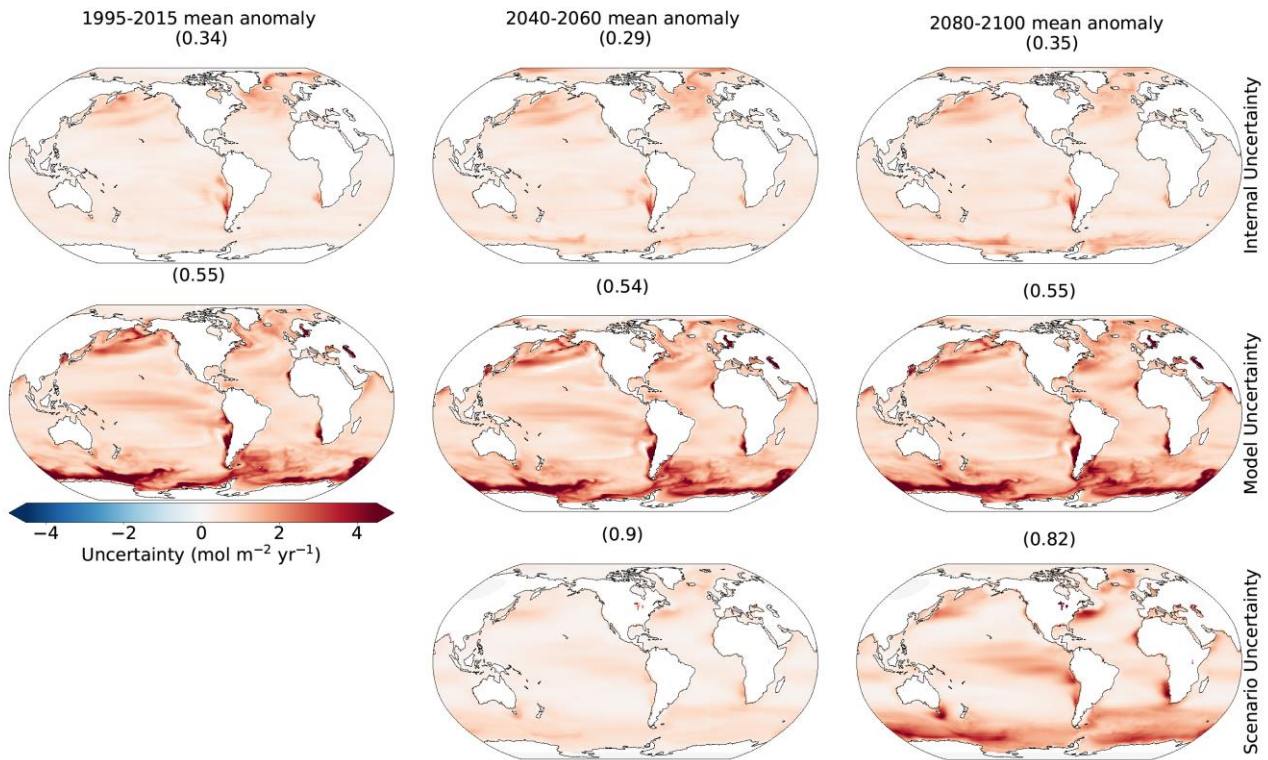
Figure 5- Sources of uncertainty averaged over the 20 year mean periods. The rows represent different sources as explained in the methods section at each grid cell. Columns represent different times: the recent (1995-2015), mid-century (2040-2060), and late-century (2080-2100) anomalies relative to the 1995-2015 mean. The numbers are correlation coefficients of each map with the 1995-2015 mean anomaly relative to the 1850-1900 mean (Fig. 1c).

518

519 3.4 Detectability

520 Detectability refers to the ability to robustly identify a forced signal, above and beyond the noise induced by internal

521 climate variability. Previous studies have largely presented a single time of emergence (Lovenduski et al. 2016,

522 Schlunegger et al., 2019, McKinley et al., 2016). However, understanding the regional differences, timescales, and

523 scenario dependence in the detectability of human induced trends in the ocean surface carbon flux is important for

524 informing observational strategies that aim to measure these changes.

525

We measure the detectability of the CMIP6 multi-model ensemble mean ocean surface carbon flux anomaly using the time of emergence at each grid point. We use this finest scale as it is the most applicable to observational communities for sampling. The time of emergence is defined as the point at which the forced signal, given by the multi-model ensemble mean flux anomaly, relative to 1995-2015, emerges from internal variability, given by the CanESM5 SMILE.

The signal in human induced surface ocean carbon flux emerges beyond the internal variability earlier in the highly active regions than anywhere else. This is evident in the Equatorial Pacific, Southern Ocean, the western boundary currents of the gyre systems, and their extensions (Fig. 6). Ocean regions such as the centres of the mid-latitude gyre systems and the NE Pacific show late emergence times and, in some cases, no detectability of the signal in any of the scenarios by 2100. Convergent large-scale circulation and strong stratification in these regions isolates the surface from the deep ocean reducing their capacity to hold large amounts of carbon (McKinley et al., 2016). An absence of mechanisms constantly drawing surface ocean CO_2 out of equilibrium with atmospheric CO_2 lets the surface water equilibrate with and adjust to the atmosphere on short time scales. Significant changes thus do not take place in the sink as the atmospheric CO_2 levels change and scenario uncertainty is lowest in the same regions (see Fig. 4). This is consistent with the results from Sect. 3.3, in which we showed that internal variability is a significant source throughout the century in the NE Pacific, with scenarios never emerging out of the range of internal variability (Fig. 4a, b). Our results for the broad patterns in the multi-model mean TOE are largely consistent with previous studies, suggesting they are robust and insensitive to for the method of estimating internal variability. These include studies from CMIP5 models such as McKinley et al., (2016) that assumed time/scenario independent internal variability, and Schlunegger et al., (2020) that used only high emission scenario internal variability from four large ensembles to show there is strong agreement between LEs TOE both locally and spatially. Our results argue for focusing observational efforts on the highly active regions in order to detect human influence on the ocean carbon sink. Meanwhile, they imply that observational timeseries in quiescent regions, such as Ocean Station Papa in the NE Pacific, need to interpret any observed trends with care, since internal variability tends to dominate over human induced trends.

555
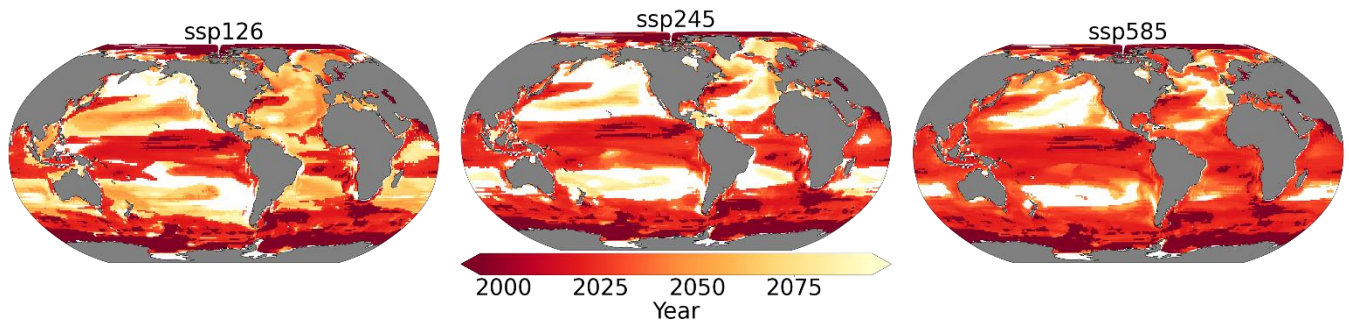
Figure 6- Time of emergence of the multi-model mean anomaly under different scenarios. White regions indicate where the anthropogenic signal cannot be detected even towards the end of the century.

Time of emergence strongly depends on the future scenario. Schlunegger et al. (2020) show for two scenarios that modest (~10 yr) TOE differences between different ESMs under strong anthropogenic forcing can evolve into pronounced (60+ yr) TOE differences with moderate mitigation. Here, we make use of three scenarios including a strong-mitigation scenario and account for scenario dependence of internal variability in our approximation using CanESM5. On average, scenarios with smaller forced trends emerge later as the size of the forced trend is critical to the time of emergence (Fig. 2-a). The TOE is earliest on average over the global ocean in ssp585, while it is later in ssp245, and later still in ssp126, consistent with the imposed changes in atmospheric CO_2 concentration. The exceptions are quiescent regions that show earlier detectability for ssp126 compared to other scenarios; these exceptions are associated with larger (but negative) anomalies in the latter half of the century under ssp126 which has negative emissions (compare panels d-f, and g-i on Fig. 1). Internal variability does evolve somewhat differently for each scenario, but this is secondary (Fig. S2). Schlunegger et al. (2020) argues that variables such as air-sea CO_2 flux which are sufficiently sensitive to emissions emerge early, prior to significant divergence among future scenarios. Consistent with this result, our results indicate that there is broad agreement between scenarios in the TOE patterns, when considering the highly active regions. Interestingly, our scenario-specific TOE shows that differences between scenario TOEs is associated with how sensitive different regions are to emission scenarios. More specifically, comparison to the maps of scenario uncertainty (Fig. 5) shows that TOE differs more across scenarios in regions where scenario uncertainty is small, such as the aforementioned subtropics Ekman convergence regions. Elsewhere, the emergence happens before scenarios diverge significantly. Our results suggest that under the rapidly rising atmospheric CO_2 concentrations seen in ssp585, the human signal in the ocean carbon sink will be detectable across much of the global ocean over the coming few decades. However, under strong mitigation scenarios, such as ssp126, early emergence (earlier than 2030) will only occur in isolated regions while counter-intuitively, less percentage of the global ocean remains non-emergent by 2100.

4. Conclusions

Ocean uptake of the increasing atmospheric CO_2 in the 21st century is concentrated in a few active regions with 70 percent of the total sink occurring in less than 40 percent of the global ocean. We analyze the results from the CMIP6 multi-model mean for the current state of the ocean (1995-2015), and the middle (2040-2060) and late (2080-2100) 21st century relative to the current state for three scenarios. We show that future changes in the sink are projected to mostly take place within the same historical highly active regions. This result implies that known regions of high historical uptake, including the North Atlantic and Southern Ocean, are the same regions to prioritize for observing the future evolution of the sink. Our results extend the argument of Wang et al. (2016) that the historical state is a good predictor of the future state to spatial patterns of change.

We show that the CMIP6 multi-model mean provides a consistent estimate of the spatial patterns of the sink, and the trend in the sink (globally), compared to the observation-based data product dataset of Landschützer et al. (2016). These results suggest the CMIP6 models are valid tools for understanding the past and future evolution of the ocean carbon sink, particularly at broad spatial scales. A notable area of disagreement is that the Landschützer et al. (2016) data shows larger decadal variability at the global scale than seen in any CMIP6 model and the range of internal variability from CanESM5 large ensemble. Gloege et al. (2021) shows that the SOM-FFN method overestimates the magnitude of decadal variability on the global scale due to the amount of gap filling.

We have shown that the magnitude of uncertainty and its partitioning among different sources differs with scale and location. On the global scale, scenario uncertainty is the largest source of uncertainty followed by model uncertainty and internal variability for CMIP6 models. These results are in agreement with previous studies form CMIP5 models (Lovenduski et al., 2016; Schlunegger et al., 2020). As the scales of integration (averaging) get finer, model and internal variability become the dominant sources, respectively. Testing the results on two ocean regions of about the same size, one in the NE Pacific and one in the NW Atlantic shows that - while consistent with the results of the scale dependence analysis - the relative importance of the sources of uncertainty also differs with location. Our test here extends the analysis Schlunegger et al. (2020) with a focus on the association of the location dependence with whether the regions have highly active carbon sinks. Notably, in highly active regions, such as the NW Atlantic, scenario uncertainty is large, whereas in more quiescent regions, such as the NE Pacific, internal variability is more significant. The dependence of internal variability on the scenario with time is another interesting finding that could be the subject of future studies for a better understanding of the driving mechanism and the degree of dependence on the future emissions and/or concentrations.

612

613   The patterns of high future CO_2 uptake uncertainty are highly correlated with the patterns of historical uptake. The

614   correlation coefficients are highest for scenario uncertainty, indicating that the highly active regions have the

615   potential for the sink to evolve according to the atmospheric CO_2 concentration, while the rest of the ocean basins

616   do not respond strongly to changes in atmospheric CO_2 represented by the different scenarios. This finding has

617   implications for assessment of the mitigations and effects of socioeconomic decisions. Our results here are

618   significant in that they show that regions of future uncertainty are largely associated with known regions of

619   significant historical uptake.

620

621   Patterns seen in the time-of-emergence have implications for planning observational campaigns for detection of a

622   signal (Schlunegger et al. 2019 & 2020). Furthermore, there is reverse association between how sensitive a region

623   is to scenario differences (apparent in the scenario uncertainty patterns) and how sensitive the TOE is to scenarios.

624   Our results show that caution should be taken in interpreting the observed changes in regions such as NE Pacific

625   associated with late time of emergence of the signal from the decadal (internal) variations. On the other hand,

626   regions such as the Equatorial Pacific, the Gulf Stream and Kuroshio and their extensions, and the Southern Ocean,

627   should be the focus of consistent and expanded sampling for detection of the forced signal. Additionally, the

628   patterns in sources of uncertainty show that model uncertainty is largest in the Southern Ocean, consistent with

629   Frölicher et al., 2015. The sink in the Southern Ocean is driven by complex mechanisms involving coupled ocean-

630   atmosphere-ice interactions that require better representation in ocean biogeochemical models. Significant progress

631   in reducing uncertainties can be expected from new methods of bringing together models and observations

632   (Frolicher et al. 2016). Our results provide a motivation to focus modelling as well as observational efforts on the

633   known highly active regions of historical uptake.

634

635   Finally, we have shown that internal variability shows clear changes in time and depends on the scenario. The

636   emergence of Large Ensembles (LEs) allows for quantification of these variations if enough ensemble members

637   are available to fully capture internal variability using realizations that start from different initial conditions. Our

638   use of the CanESM5 LE allows for us to account for the nonstationary of internal variability in time, like in

639   Schlunegger et al. (2020) but with the advantage of also accounting for scenario dependence. Model

640   intercomparison indicates that ESMs show differences in natural variability (Schlunegger et al. 2020). Nonetheless,

641   our analysis of the global scale, of scale dependence, and of the patterns seen in Time of Emergence are consistent

642   with previous studies, despite the potential sensitivity to the use of CanESM5 LE. Our methodology to correct for

643   internal variability from model spread, without filtering or having a large ensemble for each ESM (which would

limit the number of ESMs that can be included and, consequently, underestimate model uncertainty) lays the foundation for future studies when LEs are available from more ESMs and advocates for more modelling groups to provide such LEs in order to achieve an even more robust estimate of internal variability as the mean across different ESMs.

Data Availability

The data used in this study is part of the World Climate Research Programme's (WCRP) 6th Coupled Model Intercomparison Project (CMIP6) open access data. For details on accessibility see section S1 in the Supplements. The SOM-FFN data (Landschützer et al., 2017) from Landschützer (2016) can be accessed through the National Oceanographic Data Center (NODC, https://www.nodc.noaa.gov/archive/arc0105/0160558/3.3/data/0-data/) operated by the National Oceanic and Atmospheric Administration (NOAA) of the U.S. Department of Commerce.

Author Contribution

Parsa Gooya conducted the formal analysis, visualization, and original draft preparation. Conceptualization, and methodology development and validation were a collaboration of the three authors, mainly developed by Parsa Gooya with contributions from Neil Swart in development, validation, and revision and Roberta Hamme in validation and revision. Neil Swart and Roberta Hamme provided supervision and reviewing and editing of the manuscript and methodology. Funding acquisition was carried out by Roberta Hamme.

Competing of interest

The authors declare that they have no conflict of interest.

Acknowledgments

This work was supported by the Marine Carbon Sink project, funded by the Natural Sciences and Engineering Research Council of Canada through the Advancing Climate Change Science in Canada program. We thank Jim Christian for helpful suggestions on a draft of the manuscript.

References

Bopp, L., Lévy, M., Resplandy, L., and Sallée, J. B.: Pathways of anthropogenic carbon subduction in the global ocean, Geophys. Res. Lett., 42, 6416– 6423, doi:10.1002/2015GL065073, 2015.

Bushinsky, S. M., Landschützer, P., Rödenbeck, C., Gray, A. R., Baker, D., Mazloff, M. R., Resplandy, L., Johnson, K. S., and Sarmiento, J. L.: Reassessing Southern Ocean air-sea CO_2 flux estimates with the addition of biogeochemical float observations. Global Biogeochemical Cycles, 33, 1370– 1388. https://doi.org/10.1029/2019GB006176, 2019.

Canadell, J., G., Monteiro, P. M. S., Costa, M. H., Cotrim da Cunha, L., Cox, P. M., Eliseev, A. V., Henson, S., Ishii, M., Jaccard, S., Koven, C., Lohila, A., Patra, P. K., Piao, S., Rogelj, J., Syampungani, S., Zaehle, S., and Zickfeld, K.: Global Carbon and other Biogeochemical Cycles and Feedbacks. In Climate Change 2021: The Physical Science Basis. Contribution of Working Group I to the Sixth Assessment Report of the Intergovernmental Panel on Climate Change [Masson-Delmotte, V., Zhai, P., Pirani, A., Connors, S. L., Péan, C., Berger, S., Caud, N., Chen, Y., Goldfarb, L., Gomis, M. I., Huang, M., Leitzell, K., Lonnoy, E., Matthews, J. B. R., Maycock, T. K., Waterfield, T., Yelekçi, O., Yu, R., and B. Zhou (eds.)]. Cambridge University Press, Cambridge, United Kingdom and New York, NY, USA, pp. 673–816, doi:10.1017/9781009157896.007, (2021).

Ciais, P. and Sabine, C.: Carbon and other biogeochemical cycles, in Climate Change 2013: The Physical Science Basis. Contribution of Working Group I to the Fifth Assessment Report of the Intergovernmental Panel on Climate Change. Cambridge Univ. Press, 2013.

Crisp, D., Dolman, H., Tanhua, T., McKinley, G. A., Hauck, J., Bastos, A., Sitch, S., Eggleston, S., and Aich.V.: How well do we understand the land-ocean-atmosphere carbon cycle?, Reviews of Geophysics, 60, e2021RG000736. https://doi.org/10.1029/2021RG000736, 2022.

Eyring, V., Bony, S., Meehl, G. A., Senior, C. A., Stevens, B., Stouffer, R. J., and Taylor, K. E.: Overview of the Coupled Model Intercomparison Project Phase 6 (CMIP6) experimental design and organization, Geosci. Model Dev., 9, 1937–1958, https://doi.org/10.5194/gmd-9-1937-2016, 2016.

Fay, A. R. and McKinley, G. A.: Global trends in surface ocean pCO2 from in situ data. Global Biogeochemical Cycles, 27(2), 541-557, https://doi.org/10.1002/gbc.20051, 2013.

Friedrich, T., Timmermann, A., Abe-Ouchi, A., Bates, N. R., Chikamoto, M. O., and Church, M. J.: Detecting regional anthropogenic trends in ocean acidification against natural variability. Nat. Clim. Change, 2, 167–171. doi: 10.1038/nclimate1372, 2012.

Friedlingstein, P., Jones, M. W., O'Sullivan, M., Andrew, R. M., Bakker, D. C. E., Hauck, J., Le Quéré, C., Peters, G. P., Peters, W., Pongratz, J., Sitch, S., Canadell, J. G., Ciais, P., Jackson, R. B., Alin, S. R., Anthoni, P., Bates, N. R., Becker, M., Bellouin, N., Bopp, L., Chau, T. T. T., Chevallier, F., Chini, L. P., Cronin, M., Currie, K. I., Decharme, B., Djeutchouang, L., Dou, X., Evans, W., Feely, R. A., Feng, L., Gasser, T., Gilfillan, D., Gkritzalis, T., Grassi, G., Gregor, L., Gruber, N., Gürses, Ö., Harris, I., Houghton, R. A., Hurtt, G. C., Iida, Y., Ilyina, T., Luijkx, I. T., Jain, A. K., Jones, S. D., Kato, E., Kennedy, D., Klein Goldewijk, K., Knauer, J., Korsbakken, J. I., Körtzinger, A., Landschützer, P., Lauvset, S. K., Lefèvre, N., Lienert, S., Liu, J., Marland, G., McGuire, P. C., Melton, J. R., Munro, D. R., Nabel, J. E. M. S., Nakaoka, S.-I., Niwa, Y., Ono, T., Pierrot, D., Poulter, B., Rehder, G., Resplandy, L., Robertson, E., Rödenbeck, C., Rosan, T. M., Schwinger, J., Schwingshackl, C., Séférian, R., Sutton, A. J., Sweeney, C., Tanhua, T., Tans, P. P., Tian, H., Tilbrook, B., Tubiello, F., van der Werf, G., Vuichard, N., Wada, C., Wanninkhof, R., Watson, A., Willis, D.,

713   Wiltshire, A. J., Yuan, W., Yue, C., Yue, X., Zaehle, S., and Zeng, J.: Global Carbon Budget 2021, Earth Syst. Sci. Data
714   Discuss. [preprint], https://doi.org/10.5194/essd-2021-386, in review, 2021.
715
716
717   Frölicher, T. L., Sarmiento, J. L., Paynter, D. J., Dunne, J. P., Krasting, J. P., and Winton, M.: Dominance of the
718   Southern Ocean in anthropogenic carbon and heat uptake in CMIP5 models, J. Clim., 28(2), 862– 886, 2015.
719
720   Frölicher, T. L., Rodgers, K. B., Stock, C. A., and Cheung, W. W. L.: Sources of uncertainties in 21st century projections
721   of potential ocean ecosystem stressors, Global Biogeochem. Cycles, 30, 1224– 1243, doi:10.1002/2015GB005338,
722   2016.
723
724   Graven, H. D., Gruber, N., Key, R., Khatiwala, S., and Giraud, X.: Changing controls on oceanic radiocarbon: New
725   insights on shallow-to-deep ocean exchange and anthropogenic CO_2 uptake, J. Geophys. Res.-Oceans, 117,
726   C10005, https://doi.org/10.1029/2012JC008074, 2012.
727
728   Gloege, L., McKinley, G. A., Landschützer, P., Fay, A. R., Frölicher, T. L., Fyfe, J. C., et al.: Quantifying errors in
729   observationally based estimates of ocean carbon sink variability. Global Biogeochemical Cycles, 35,
730   doi:10.1029/2020GB006788, 2021.
731
732   Gray, A. R., Johnson, K. S., Bushinsky, S. M., Riser, S. C., Russell, J.L., Wanninkhof, R., Williams, N. L., and
733   Sarmiento, J. L.: Autonomous biogeochemical floats detect significant carbon dioxide outgassing in the high-latitude
734   Southern Ocean, Geophys. Res. Lett., 45, 9049–57, 2018.
735
736   Gruber, N., Landschützer, P., and Lovenduski, N. S.: The Variable Southern Ocean Carbon Sink, Annual Review of
737   Marine Science, 11:1, 159-186, 2019.
738
739   Hauck, J., Völker, C., Wolf-Gladrow, D. A., Laufkötter, C., Vogt, M., Aumont, O., Bopp, L., Buitenhuis, E. T., Doney,
740   S. C., Dunne, J., Gruber, N., Hashioka, T., John, J., Le Quéré, C., Lima, I. D., Nakano, H., Séférian, R., Totterdell, I.: On
741   the Southern Ocean CO_2 uptake and the role of the biological carbon pump in the 21st century, Global Biogeochem.
742   Cycles, 29, 1451– 1470, doi:10.1002/2015GB005140, 2015.
743
744   Hauck J., Zeising M., Le Quéré C., Gruber N., Bakker D. C. E., Bopp L., Chau T. T. T., Gürses Ö., Ilyina T.,
745   Landschützer P., Lenton A., Resplandy L., Rödenbeck C., Schwinger J. and Séférian R.: Consistency and Challenges in
746   the Ocean Carbon Sink Estimate for the Global Carbon Budget. Front. Mar. Sci. 7:571720. doi:
747   10.3389/fmars.2020.571720, 2020.
748
749   Hawkins, E. and Sutton, R.: The potential to narrow uncertainty in regional climate predictions. Bull. Am. Meteorol.
750   Soc., 90:1095, 2009.
751
752   Hawkins, E. and Sutton, R. Time of emergence of climate signals. Geophys. Res. Lett. 39, L01702, 2012.
753
754
755   Joos, F. and Spahni, R.: Rates of change in natural and anthropogenic radiative forcing over the past 20,000 years.
756   Proceedings of the National Academy of Sciences of the United States of America, 105, 1425-30, 2008.
757
758
759   Kumar, D. and Ganguly, A. R.: Intercomparison of model response and internal variability across climate model
760   ensembles, Clim. Dynam., 51, 207–219, https://doi.org/10.1007/s00382-017-3914-4, 2018.
761

Landschützer, P., Gruber, N., Haumann, F. A., Rödenbeck, C., Bakker, D. C., Van Heuven, S., Hoppema M., Metzl N., Sweeney C., Takahashi T., Tilbrook B., Wanninkhof R.: The reinvigoration of the Southern Ocean carbon sink. Science, 349(6253), 1221–1224, 2015.

Landschützer, P., Gruber, N., and Bakker, D. C. E.: Decadal variations and trends of the global ocean carbon sink, Global Biogeochem. Cycles, 30, 1396– 1417, doi:10.1002/2015GB005359, 2016.

Landschützer, P., Gruber N., and Bakker, D.C.E.: An updated observation-based global monthly gridded sea surface pCO2 and air-sea CO2 flux product from 1982 through 2015 and its monthly climatology (NCEI Accession 0160558), Version 2.2, NOAA National Centers for Environmental Information, Dataset, 2017.

Laufkötter, C., Vogt, M., Gruber, N., Aita-Noguchi, M., Aumont, O., Bopp, L., Buitenhuis, E., Doney, S. C., Dunne, J., Hashioka, T., Hauck, J., Hirata, T., John, J., Le Quéré, C., Lima, I. D., Nakano, H., Seferian, R., Totterdell, I., Vichi, M., and Völker, C.: Drivers and uncertainties of future global marine primary production in marine ecosystem models, Biogeosciences, 12, 6955–6984, https://doi.org/10.5194/bg-12-6955-2015, 2015.

Lehner, F., Deser, C., Maher, N., Marotzke, J., Fischer, E. M., Brunner, L., Knutti, R., and Hawkins, E.: Partitioning climate projection uncertainty with multiple large ensembles and CMIP5/6, Earth Syst. Dynam., 11, 491–508, https://doi.org/10.5194/esd-11-491-2020, 2020.

Lorenz E. N.: The predictability of a flow which possesses many scales of motion., Tellus, ;21:19, 1969.

Lovenduski, N. S., Gruber, N., Doney, S. C., and Lima, I. D.: Enhanced CO2 outgassing in the Southern Ocean from a positive phase of the Southern Annular Mode. Global Biogeochemical Cycles, 21(2). https://doi.org/10.1029/2006GB002900, 2007.

Lovenduski, N. S., McKinley, G. A., Fay, A. R., Lindsay, K., and Long, M. C.: Partitioning uncertainty in ocean carbon uptake projections: Internal variability, emission scenario, and model structure, Global Biogeochem. Cycles, 30, 1276– 1287, 2016.

Masson-Delmotte, V., P. Zhai, A. Pirani, S.L. Connors, C. Péan, S. Berger, N. Caud, Y. Chen, L. Goldfarb, M.I. Gomis, M. Huang, K. Leitzell, E. Lonnoy, J.B.R. Matthews, T.K. Maycock, T. Waterfield, O. Yelekçi, R. Yu, and B. Zhou (eds.): IPCC, 2021: Summary for Policymakers. In: Climate Change 2021, The Physical Science Basis. Contribution of Working Group I to the Sixth Assessment Report of the Intergovernmental Panel on Climate Change. In Press.

McKinley G. A., Pilcher D. J., Fay A. R., Lindsay K., Long M. C., and Lovenduski N. S.: Timescales for detection of trends in the ocean carbon sink. Nature, 530(7591), 469-72. doi: 10.1038/nature16958. PMID: 26911782, 2016.

McKinley, G. A., Fay, A. R., Lovenduski, N. S., and Pilcher, D.: Natural variability and anthropogenic trends in the ocean carbon sink. Annual Review of Marine Science, 9(1), 125–150. https://doi.org/10.1146/annurev-marine-010816-060529, 2017.

McKinley, G. A., Fay, A. R., Eddebbar, Y. A., Gloege, L., and Lovenduski, N. S.: External forcing explains recent decadal variability of the ocean carbon sink. AGU Advances, 1, e2019AV000149. https://doi.org/10.1029/2019AV000149, 2020.

Riahi, K., van Vuuren, D. P., Kriegler, E., Edmonds, J., O'Neill, B. C., Fujimori, S., Bauer, N., Calvin, K., Dellink, R., Fricko, O., Lutz, W., Popp, A., Cuaresma, J. C., KC, S., Leimbach, M., Jiang, L., Kram, T., Rao, S., Emmerling, J., Ebi, K., Hasegawa, T., Havlik, P., Humpenöder, F., Aleluia Da Silva, L., Smith, S., Stehfest, E., Bosetti, V., Eom, J., Gernaat, D., Masui, T., Rogelj, J., Strefler, J., Drouet, L., Krey, V., Luderer, G., Harmsen, M., Takahashi, K., Baumstark, L., Doelman, J. C., Kainuma, M., Klimont, Z., Marangoni, G., Lotze-Campen, H., Obersteiner, M., Tabeau, A., and Tavoni, M.: The Shared Socioeconomic Pathways and their energy, land use, and greenhouse gas emissions implications: An overview, Global Environmental Change, Volume 42, 153-168, ISSN 0959-3780, https://doi.org/10.1016/j.gloenvcha.2016.05.009, 2017.

Ridge, S. M. and McKinley, G. A.: Ocean carbon uptake under aggressive emission mitigation, Biogeosciences, 18, 2711–2725, https://doi.org/10.5194/bg-18-2711-2021, 2021.

Rodgers, K. B., Lin, J. and Frolicher, T. L.: Emergence of multiple ocean ecosystem drivers in a large ensemble suite with an Earth system model. Biogeosciences, 12, 3301–3320, 2015.

Roy, T., L. Bopp, M. Gehlen, B. Schneider, P. Cadule, T. L. Frölicher, J. Segschneider, J. Tjiputra, C. Heinze, and F. Joos: Regional impacts of climate change and atmospheric CO_2 on future ocean carbon uptake: A multimodel linear feedback analysis, J. Clim., 24(9), 2300– 2318, 2011.

Santer, B.D., P.W. Thorne, L. Haimberger, K.E. Taylor, T.M.L. Wigley, J.R. Lanzante, S. Solomon, M. Free, P.J. Gleckler, P.D. Jones, T.R. Karl, S.A. Klein, C. Mears, D. Nychka, G.A. Schmidt, S.C. Sherwood, and F.J. Wentz: Consistency of modelled and observed temperature trends in the tropical troposphere. Int. J. Climatol., 28, 1703-1722, doi:10.1002/joc.1756, 2008.

Sarmiento, J. L., Hughes, T. M. C., Stouffer, R. J., and Manabe, S.: Simulated response of the ocean carbon cycle to anthropogenic climate warming. Nature, 393(6682), 245–249. https://doi.org/10.1038/30455, 1998.

Schlunegger, S., Rodgers, K. B., Sarmiento, J. L., Frölicher, T. L., Dunne, J. P., Ishii, M., and Slater, R.: Emergence of anthropogenic signals in the ocean carbon cycle. Nature Climate Change, 9(9), 719–725. https://doi.org/10.1038/s41558-019-0553-2, 2019.

Schlunegger, S., Rodgers, K. B., Sarmiento, J. L., Ilyina, T., Dunne, J. P., Takano, Y., Christian, J. R., Long, M. C., Frölicher, T. L., Slater, R., and Lehner, F.: Time of Emergence and Large Ensemble Intercomparison for Ocean Biogeochemical Trends. Global Biogeochemical Cycles, 34(8), e2019GB006453. https://doi.org/https://doi.org/10.1029/2019GB006453, 2020.

Somerville, R.C.J.: The predictability of weather and climate. Climatic Change 11, 239–246, https://doi.org/10.1007/BF00138802, 1987.

Sutton AJ, Wanninkhof R, Sabine CL, Feely RA, Cronin MF, Weller RA. 2017. Variability and trends in surface seawater pCO 2 and CO 2 flux in the Pacific Ocean. Geophys Res Lett, 44(11): 5627–5636. doi: 10.1002/2017GL073814

854 Takahashi T., Sutherland S. C., Feely R.A., Wanninkhof R.: Decadal change of the surface water pCO_2 in the North
855 Pacific: A synthesis of 35 years of observations. J Geophys Res, 111(C7): C07S05. doi: 10.1029/2005JC003074, 2006.

856
857 Tebaldi C. and Knutti R.: The use of the multimodel ensemble in probabilistic climate projections. Phil. Trans. R. Soc.
858 A., 365, 2053–2075, 2007.

859
860 Terhaar, J., Frölicher, T. L., and Joos, F.: Southern Ocean anthropogenic carbon sink constrained by sea surface
861 salinity. Science Advances, 7(18), eabd5964. https://doi.org/10.1126/sciadv.abd5964, 2021.

862
863 Tjiputra, J. F., Olsen, A., Bopp, L., Lenton, A., Pfeil, B., Roy, T., Segschneider, J., Totterdell, I., and Heinze, C.: Long-
864 term surface pCO_2 trends from observations and models, Tellus B., 66, 23083, 2014.
865
866 Toyama, K., Rodgers, K. B., Blanke, B., Iudicone, D., Ishii, M., Aumont, O., and Sarmiento, J. L.: Large Reemergence
867 of Anthropogenic Carbon into the Ocean's Surface Mixed Layer Sustained by the Ocean's Overturning Circulation, J.
868 Climate, 30, 8615–8631, https://doi.org/10.1175/JCLI-D-16-0725.1, 2017.
869
870
871 Wang, L., Huang, J., Luo, Y., and Zhao, Z.: Narrowing the spread in CMIP5 model projections of air-sea CO2
872 fluxes. Scientific Reports, 6(1), 37548. https://doi.org/10.1038/srep37548, 2016.

873
874 Williams, N. L., Juranek, L. W., Feely, R. A., Russell, J. L., Johnson, K. S., and Hales, B.: Assessment of the carbonate
875 chemistry seasonal cycles in the Southern Ocean from persistent observational platforms. J. Geophys. Res. Oceans,
876 123,4833–52, 2018.
877